

# Acoustic standing wave modulation of capacitively coupled plasmas

Bocong Zheng<sup>1</sup> , Thomas Schuelke<sup>1,2</sup> and Qi Hua Fan<sup>1,2,3</sup>

<sup>1</sup> Fraunhofer Center for Coatings and Diamond Technologies, Michigan State University, East Lansing, MI 48824, United States of America

<sup>2</sup> Department of Electrical and Computer Engineering, Michigan State University, East Lansing, MI 48824, United States of America

<sup>3</sup> Department of Chemical Engineering and Materials Science, Michigan State University, East Lansing, MI 48824, United States of America

E-mail: [qfan@egr.msu.edu](mailto:qfan@egr.msu.edu)

Received 9 April 2018, revised 29 May 2018

Accepted for publication 5 June 2018

Published 22 June 2018



## Abstract

This work presents a concept of using acoustic standing waves to modulate plasmas. A 1D self-consistent fluid model combined with an acoustic standing wave model has been established to investigate the strong coupling effects between acoustic standing waves and capacitively coupled argon plasmas. The modulation effects are revealed by comparing the spatiotemporal distributions of electron density and excited species number density with and without the acoustic standing waves in one acoustic period, as well as the electric field, the electron temperature, the ionization and excitation rates, and the power density in one radio-frequency period. Under the nonlinear acoustic standing waves, the plasmas oscillate in between the electrodes, which indicates a strong modulation effect beyond conventional regimes. This modulation effect is primarily attributed to the neutral flux friction to the plasma species and secondarily to the variation of the neutral gas density. A pulsed excited species flux with a maximum value up to twice of the minimum can be achieved at the electrodes as a result of the acoustic standing wave modulation. The distributions of the ionization and excitation rates in one RF period are significantly influenced by the acoustic standing waves, due to the variation of the neutral gas density and electron temperature. This study initiates the effort to understand the mechanisms and characteristics of plasma discharges in a high-intensity acoustic standing wave field. Using acoustic waves to modulate plasmas has the potential to create many new applications and promote plasma-materials interactions.

Keywords: capacitively coupled plasma, acoustic standing wave, plasma simulation

(Some figures may appear in colour only in the online journal)

## 1. Introduction

Low-temperature plasmas play critical roles in materials processing and nanotechnologies [1]. The efficiency of plasma-materials interactions strongly depends on the transport rates of the reactive species to the working surfaces and the plasma distribution. In conventional discharges, the plasmas reach steady state rapidly. The strong charge neutrality and a shielding effect tightly hold the bulk plasma in the discharge region. Hence, the electric field in the bulk plasma region is very low; the electric potential is only  $\sim T_e/2$  (a few volts)

in the plasma and zero at the sheath edge. As a result, the drift velocity of the charged particles in the bulk plasma is almost negligible until they enter the narrow sheath region. Consequently, the excited species follow the distribution of the charged particles and undergo random Brownian motion. In general, the distributions of plasma species (ion and excited species) are determined by the discharge characteristics and are stable over time.

Modulating the distributions of plasmas is scientifically interesting and practically attractive as it could result in unusual effects that promote the efficiency of plasma processing.

Multiple benefits have been demonstrated with pulsed plasmas driven by time-modulated bias applied to the working electrodes and/or substrates [2]. Some favorable effects include enhanced plasma uniformity [3, 4], controlled ion energy [5], tunable chemical composition [6], improved density and smoothness of deposited films [7], and increased deposition rate [8]. However, the variations in the spatiotemporal distributions of the plasmas under pulsed modulations are in fact very limited due to the ‘collective behavior’ of plasmas that resist the external influences [9]. In other words, the movement of charged particles in a plasma generates local net charges and currents, giving rise to long-range electromagnetic forces that restrict the plasmas’ response to the external electric fields, the bulk plasma remains nearly unaffected. In addition, the excited chemical species produced by the plasmas are of great importance in interacting with materials. The electrohydrodynamic flows generated by corona [10, 11] and surface dielectric barrier discharges [12] have been used to modulate the spatial distribution of the chemical species and control the neutral flows of the plasmas. However, the maximum speed of an electrohydrodynamic flow is only a few meters per second [13], which can very much affect the long-lived species but have little effect on the excited species [11]. Therefore, if the plasma distribution could be modulated over a large scale, it would create new effects and process regimes that lead to significantly enhanced gas-phase reactions and plasma-materials interactions.

This work presents a new concept of using acoustic standing waves to modulate plasmas. The purpose is to realize large-scale modulation of the reactive species (ions and excited particles) in plasmas beyond the conventional regimes. Under an acoustic field, neutral gas particles undergo periodic directional movements, creating strong neutral flows and friction forces [14, 15]. The local collisions between the background neutral gases and the ions/active species could efficiently modulate the plasma distributions if the acoustic field is sufficiently strong. It has been reported that high-intensity, nonlinear acoustic standing waves with peak acoustic pressures up to 3–4 times of the background pressure can be excited [16]. Under such high-amplitude acoustic standing waves, the fluxes of active species to the substrate could be strongly modulated due to the collision friction effect of the neutral gases driven by the acoustic waves.

This work initiates the effort to understand the strong coupling effects between the acoustic standing waves and capacitively coupled plasmas (CCP) that are most widely used for materials processing. A force field induced by the high-intensity acoustic standing waves is integrated into a plasma discharge model. Numerical simulation is performed to correlate the plasma properties with the acoustic standing waves. The studies particularly focus on revealing the spatiotemporal distributions of the plasmas under the modulation of nonlinear acoustic standing waves. The periodically increased transport rates of plasma species are predicted to possess sharp pulses that could not be achieved with conventional methods. Some potential applications of acoustic wave modulated plasmas are indicated with the aim to stimulate further studies in this new research area.

## 2. Model description

This section describes a 1D fluid model that combines CCP discharge with a high-intensity acoustic standing wave field. This model is subsequently used to investigate the influence of acoustic standing waves on the plasma discharge dynamics. Since the research focuses on the coupling between the plasma and acoustic waves, argon gas is selected as the working gas to simplify the simulation and the complex gas mixtures used in a variety of applications will be investigated in further studies. In argon discharges, the primary species include neutral argon atoms ( $\text{Ar}$ ), singly charged argon ions ( $\text{Ar}^+$ ), metastable argon species ( $\text{Ar}^m$ ) and electrons ( $e$ ). At a typical CCP working pressure of 1 Torr, the background Ar gas and the generated plasmas can be regarded as continuous media and described by fluid approach. The nonuniform acoustic pressure would influence the ionization and excitation processes, which are proportional to the neutral gas density, and the particle velocities in the acoustic field could produce a significant friction force to the ionized and activated species. Since the typical frequency (13.56 MHz) for a CCP discharge is much higher than the acoustic frequency (typically in the range of kHz), the neutral gas distribution can be assumed to be steady for the discharge process. Therefore, the acoustic field is one-way coupled to the plasma discharge, which means that the nonuniform acoustic pressure and particle velocity obtained from an acoustic standing wave model will be used as the input parameters for the plasma discharge model. The acoustic standing wave model and the plasma discharge model are described below.

### 2.1. The acoustic standing wave model

The wave pressure created by low-amplitude acoustic standing waves is small compared to the background pressure. Therefore, a linearization approximation can be used to obtain a sinusoidal distribution of the acoustic pressure and particle velocity. However, the acoustic waves with sufficiently large amplitudes will be distorted as they travel, and the nonlinearity effects cannot be ignored. A 1D wave equation is derived from the mass conservation equation, the momentum conservation equation, and the state equation. This wave equation, which contains up to the third-order terms [17, 18], is used here to describe the motion of neutral gases as well as the high-amplitude acoustic field in a constant cross sectioned chamber as follows:

$$\begin{aligned} c^2 \frac{\partial^2 \varphi}{\partial x^2} - \frac{\partial^2 \varphi}{\partial t^2} + \delta \frac{\partial^3 \varphi}{\partial x^2 \partial t} &= \frac{da}{dt}x + a \frac{\partial \varphi}{\partial x} \\ &+ (\gamma - 1)ax \frac{\partial^2 \varphi}{\partial x^2} + 2 \frac{\partial \varphi}{\partial x} \frac{\partial^2 \varphi}{\partial x \partial t} + (\gamma - 1) \frac{\partial \varphi}{\partial t} \frac{\partial^2 \varphi}{\partial x^2} \\ &+ \frac{\gamma + 1}{2} \left( \frac{\partial \varphi}{\partial x} \right)^2 \frac{\partial^2 \varphi}{\partial x^2}, \end{aligned} \quad (1)$$

where  $\varphi$  is the velocity potential,  $x$  is the spatial axis along the wave propagating direction,  $t$  is the time,  $c$  is the small signal propagation speed,  $\delta = (\zeta + 4\eta/3)/\rho_0$  is the attenuation

constant,  $\rho_0$  is the ambient fluid density,  $\zeta$  and  $\eta$  are the bulk and shear viscosities, respectively,  $a = a_0 \sin(f_a t)$  is the acceleration of the acoustic source,  $a_0$  and  $f_a$  are the amplitude and frequency of the acoustic source, and  $\gamma$  is the heat capacity ratio of the background gas. The first two terms on the left-hand side of equation (1) are the linear lossless wave equation and the third term describes the viscous volume attenuation. The first three terms on the right-hand side are the acceleration terms, the fourth and fifth terms are the second-order nonlinear terms and the last one is a third-order nonlinear term. The boundary conditions for equation (1) are  $\frac{\partial \varphi}{\partial x}|_{x=0} = \frac{\partial \varphi}{\partial x}|_{x=l} = 0$ , where  $l$  is the distance between the two parallel electrode plates. By setting the initial conditions as  $\varphi|_{t=0} = \frac{\partial \varphi}{\partial t}|_{t=0} = 0$ , a periodically steady state could be achieved after several acoustic periods. Once equation (1) is numerically solved and the velocity potential  $\varphi$  is obtained, the acoustic pressure  $p$  and the particle velocity  $u_n$  can be calculated as

$$\begin{aligned} p &= p_0 \left( 1 - \frac{\gamma - 1}{c^2} \left[ \frac{\partial \varphi}{\partial t} + \frac{1}{2} \left( \frac{\partial \varphi}{\partial x} \right)^2 + ax - \delta \frac{\partial^2 \varphi}{\partial x^2} \right] \right)^{\gamma/(\gamma-1)} \\ u_n &= \frac{\partial \varphi}{\partial x}, \end{aligned} \quad (2)$$

where  $p_0$  is the background pressure. Using the above equations, the nonlinear acoustic standing waves in a symmetric chamber can be described, whose validity has been experimentally verified [16]. The acoustic pressure and particle velocity obtained from equation (2) are set as the input parameters of the plasma discharge model.

## 2.2. The plasma discharge model

The built-in plasma module of the commercial software COMSOL [19] is used to establish the plasma discharge model and some of the embedded equations are modified to incorporate the influence of the nonuniform acoustic pressure and particle velocity. The species considered in the argon plasmas are electrons,  $\text{Ar}^+$  and  $\text{Ar}^m$ . The electrons can be described by the continuity equation and the energy conservation equation. Since the neutral gas has a velocity distribution  $u_n$  induced by the acoustic standing waves, the mass balance of electrons can be described by the continuity equation as

$$\frac{\partial n_e}{\partial t} + \nabla \cdot (\Gamma_e + n_e u_n) = R_e, \quad (3)$$

where  $n_e$  is the electron density,  $\Gamma_e$  is the drift-diffusion flux of electrons,  $n_e u_n$  is the advection flux induced by the neutral gas friction and  $R_e$  is the ionization rate. The velocity in the advection flux term is contributed by the bulk fluid motion, that is, the velocity of the background neutral gas that the particles are moving with, which is  $u_n$ . In the case of electrons, the advection flux term can usually be neglected, since the electron velocity contributed by the drift-diffusion term is much greater than  $u_n$ . Substituting the drift-diffusion approximation  $\Gamma_e = -\mu_e E n_e - \nabla(D_e n_e)$  into the electron

continuity equation and expanding the advection term, the above equation becomes

$$\frac{\partial n_e}{\partial t} + \nabla \cdot (-\mu_e E n_e - \nabla(D_e n_e)) + (u_n \cdot \nabla) n_e + n_e \nabla \cdot u_n = R_e, \quad (4)$$

where  $R_e = \sum_j k_{iz,j} n_j n_e$ ,  $k_{iz,j}$  is the ionization rate coefficient of electron collisions with species  $j$ ,  $n_j$  is the number density of species  $j$ ,  $E$  is the electric field,  $D_e = \mu_e T_e$  is the diffusion coefficient of electrons calculated from Einstein's relationship, and  $\mu_e p = 30$  ( $\text{m}^2 \text{V}^{-1} \cdot \text{s}$ ) Torr is the reduced electron mobility [20].

The energy balance equation of electrons has a similar form to equation (3),

$$\frac{\partial n_e}{\partial t} + \nabla \cdot (\Gamma_e + n_e u_n) + E \cdot \Gamma_e = Q, \quad (5)$$

where  $n_e = \frac{3}{2} n_e T_e$  is the electron energy density,  $\Gamma_e = -\mu_e E n_e - \nabla(D_e n_e)$  is the electron energy flux,  $\mu_e = \frac{5}{3} \mu_e$  and  $D_e = \frac{5}{3} D_e$  are the electron energy mobility and diffusion coefficient,  $n_e u_n$  is the advection flux of electron energy,  $E \cdot \Gamma_e$  represents heating by the electric field, and  $Q = \sum_j k_j n_j n_e \Delta \epsilon_j$  is the energy variation due to polarization scattering and inelastic collisions.  $k_j$  and  $\Delta \epsilon_j$  are the rate coefficient and the energy variation of elastic and inelastic collisions between electron and species  $j$ . By substituting these terms into equation (5), we have

$$\frac{\partial}{\partial t} \left( \frac{3}{2} n_e T_e \right) + \nabla \cdot \left( \frac{5}{2} T_e \Gamma_e - \frac{5}{2} n_e D_e \nabla T_e + \frac{3}{2} n_e T_e u_n \right) + E \cdot \Gamma_e = Q. \quad (6)$$

Similar to the electrons, the continuity equations of heavy species  $\alpha$  can be derived as

$$\frac{\partial n_\alpha}{\partial t} + \nabla \cdot (\Gamma_\alpha + n_\alpha u_n) = R_\alpha, \quad (7)$$

where  $\alpha = \text{Ar}^m, \text{Ar}^+$ ,  $n_\alpha$  and  $\Gamma_\alpha = z_\alpha \mu_\alpha E n_\alpha - \nabla(D_\alpha n_\alpha)$  are the number density and the diffusion flux of  $\alpha$ ,  $z$  is the charge number,  $n_\alpha u_n$  is the neutral-gas-friction-induced advection flux of heavy species,  $R_\alpha$  is the rate expression for species  $\alpha$ . The diffusion coefficient of  $\text{Ar}^+$  is adopted as  $D_{\text{Ar}^+} = \frac{k_B T_{\text{Ar}^+}}{m_i \nu_i}$  [1],  $k_B$  is the Boltzmann constant,  $m_i$  is the mass of Ar ion, the Ar ion temperature  $T_{\text{Ar}^+}$  is set as equal to the gas temperature, and  $\nu_i = \sigma_i \bar{v}_i n_{\text{Ar}}$  is the ion-neutral collision frequency, where  $\sigma_i$  is considered as a constant of  $5 \times 10^{-19} \text{ m}^2$  [21] and  $\bar{v}_i = \sqrt{8k_B T_{\text{Ar}^+}/\pi m_i}$  is the ion thermal velocity. The corresponding ion mobility is calculated from Einstein's relation. The reduced diffusion coefficient for  $\text{Ar}^m$  is set as  $D_{\text{Ar}^m} n_{\text{Ar}} = 2.42 \times 10^{20} \text{ m}^{-1} \text{ s}^{-1}$  [22]. In this study, the drift-diffusion approximation is adopted to solve the fluxes instead of the equation of motion to simplify the model. For RF discharges, the drift-diffusion approximation is acceptable when the working pressure is greater than about 500 mTorr [20].

The electric field  $E = \partial \phi / \partial x$  is obtained by solving the Poisson's equation,

$$\nabla^2 \phi = \frac{e}{\epsilon_0} (n_i - n_e), \quad (8)$$

**Table 1.** Principal rate coefficients for the Ar plasma.

| Reaction                                       | Rate coefficient ( $\text{m}^3 \text{s}^{-1}$ )  | Threshold (eV) | Reference |
|--|--|----------------|-----------|
| $e + \text{Ar} \rightarrow e + \text{Ar}$      | $2.336 \times 10^{-14} T_e^{1.609} \times \exp(0.0618(\ln T_e)^2 - 0.1171(\ln T_e)^3)$ |                | [1]       |
| $e + \text{Ar} \rightarrow 2e + \text{Ar}^+$   | $2.34 \times 10^{-14} T_e^{0.59} \exp(-17.44/T_e)$                                     | 15.76          | [23]      |
| $e + \text{Ar} \rightarrow e + \text{Ar}^m$    | $2.5 \times 10^{-15} T_e^{0.74} \exp(-11.56/T_e)$                                      | 11.56          | [24]      |
| $e + \text{Ar}^m \rightarrow e + \text{Ar}$    | $4.3 \times 10^{-16} T_e^{0.74}$   | -11.56         | [25]      |
| $e + \text{Ar}^m \rightarrow 2e + \text{Ar}^+$ | $6.8 \times 10^{-15} T_e^{0.67} \exp(-4.2/T_e)$  | 4.2            | [26]      |

where  $\phi$  is the electric potential and  $\epsilon_0$  is the permittivity of free space. The rate coefficients used in the model are shown in table 1. For plasmas with a relatively high pressure plasma used in this model, the electron energy distribution function (EEDF) is assumed as Maxwellian.

The boundary conditions for the plasma discharge model are as follows: one of the electrodes is set to be grounded as  $\phi|_{x=0} = 0$ , and another electrode is connected to a RF source with voltage amplitude  $V_{\text{RF}}$  and frequency  $f_{\text{RF}}$  as  $\phi|_{x=l} = V_{\text{RF}} \sin(2\pi f_{\text{RF}} t)$ . The electron flux at the electrodes is  $\Gamma_e = \frac{1}{4} n_e \sqrt{8T_e/\pi m_e}$ , and the corresponding electron energy flux is  $\frac{5}{2} T_e \Gamma_e$ . The flux of heavy species at the electrodes is calculated from [27]

$$\Gamma_\alpha = \frac{\gamma_\alpha}{1 - \gamma_\alpha/2} \frac{1}{4} n_\alpha \sqrt{\frac{8k_B T_\alpha}{\pi m_\alpha}} + z_\alpha \mu_\alpha E n_\alpha, \quad (9)$$

where  $\gamma_\alpha = 1$  is the sticking coefficient,  $\sqrt{8k_B T_\alpha/\pi m_\alpha}$  is the averaged thermal velocity of heavy species  $\alpha$ .

### 3. Results and discussion

Using the acoustic standing wave model and the plasma discharge model described above, CCP discharges modulated by acoustic standing waves are numerically studied. The schematic diagram of the CCP discharge reactor with an acoustic source applied to the left electrode plate is illustrated in figure 1. To simplify the simulation of the acoustic standing wave, the chamber is assumed to have a plane cross section in the direction perpendicular to the electrodes. The background pressure and the gap length between the electrode plates are set as  $p_0 = 1$  Torr and  $l = 2.54$  cm, respectively, corresponding to the typical CCP discharge conditions. The parameters adopted in the acoustic standing wave model and the plasma discharge model are as follows. The small signal propagation speed is  $c = \sqrt{\gamma k_B T_{\text{Ar}}/m_{\text{Ar}}}$ , where the heat capacity ratio  $\gamma$  for monatomic Ar is 5/3 and the gas temperature of heavy species  $T_{\text{Ar}}$  is kept as 400 K. The bulk and shear viscosities of Ar are set as  $\zeta = 0$  (for dilute monatomic gases) [28, 29] and  $\eta = 22.9 \mu\text{Pa} \cdot \text{s}$  [30, 31], respectively. To achieve the largest acoustic wave amplitude with a given input power, the angular frequency of the acoustic source  $\omega_a = 2\pi f_a$  is set to the lowest mode angular frequency  $\omega_a = \pi c/l$  [17] of a cylindrical resonator of length  $l$ . In this case, an acoustic standing wave with a frequency of  $f_a \approx 7.9$  kHz and a wavelength of  $2l$  could be produced in the chamber, with one pressure node at the center point  $x = l/2$ , and two antinodes at the

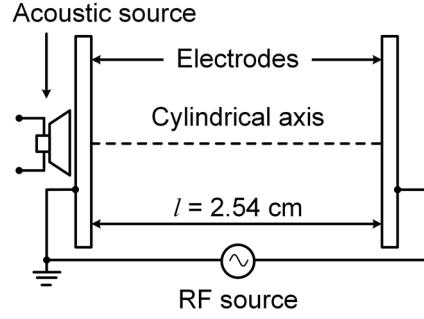


**Figure 1.** Schematic diagram of the CCP discharge reactor with an acoustic source.

electrode plate boundaries  $x = 0$  and  $x = l$ . The acceleration amplitude is  $a_0 = \delta_0 \omega_a^2$ , where  $\delta_0$  is the vibration amplitude of the acoustic source and is set as 200  $\mu\text{m}$  in the simulation of plasma discharge processes. The RF source frequency and voltage are  $f_{\text{RF}} = 13.56$  MHz and  $V_{\text{RF}} = 200$  V, respectively. The following discussion is based on the simulation results after the calculation of 100 acoustic periods (or 172 500 RF periods), approximately 13 ms. Albeit the time may not be sufficient for the discharge system to achieve perfect steady state, it is believed that the simulation results provided below are close to the final state and the primary physics has been sufficiently incorporated in the model.

The spatiotemporal variation profiles of the acoustic pressures and the particle velocities are simulated by the acoustic standing wave model at the above conditions. The simulation results are illustrated within one acoustic standing wave period at different vibration amplitudes of the acoustic source, as shown in figure 2. At low intensity of the acoustic standing waves (figure 2(a)), the variations of the acoustic pressure and the particle velocity are relatively small, less than 1% and 2  $\text{m s}^{-1}$ , respectively, and both have a sinusoidal-like profile. Since the acoustic field is at its lowest mode, one pressure node is formed at the center of the chamber and two antinodes at the electrode boundaries. For the particle velocity, two nodes are formed at the boundaries and one antinode is formed at the center of the chamber. However, as the vibration amplitude  $\delta_0$  increases from 1 to 200  $\mu\text{m}$ , a nonlinear effect begins to play an important role and the wave profiles deviate from the sinusoidal form (figures 2(b)–(d)). The cumulative effect of the wave distortion leads to highly nonlinear variation of the propagation velocity [32], the peaks of the wave travel faster than the troughs. The eventual self-distorted waves have a sawtooth profile (figure 2(d)). At a vibration amplitude of 200  $\mu\text{m}$ , the variation range of the pressure is from 74.3 to 210 Pa, about 57% of the base pressure of 133 Pa, and the maximal particle

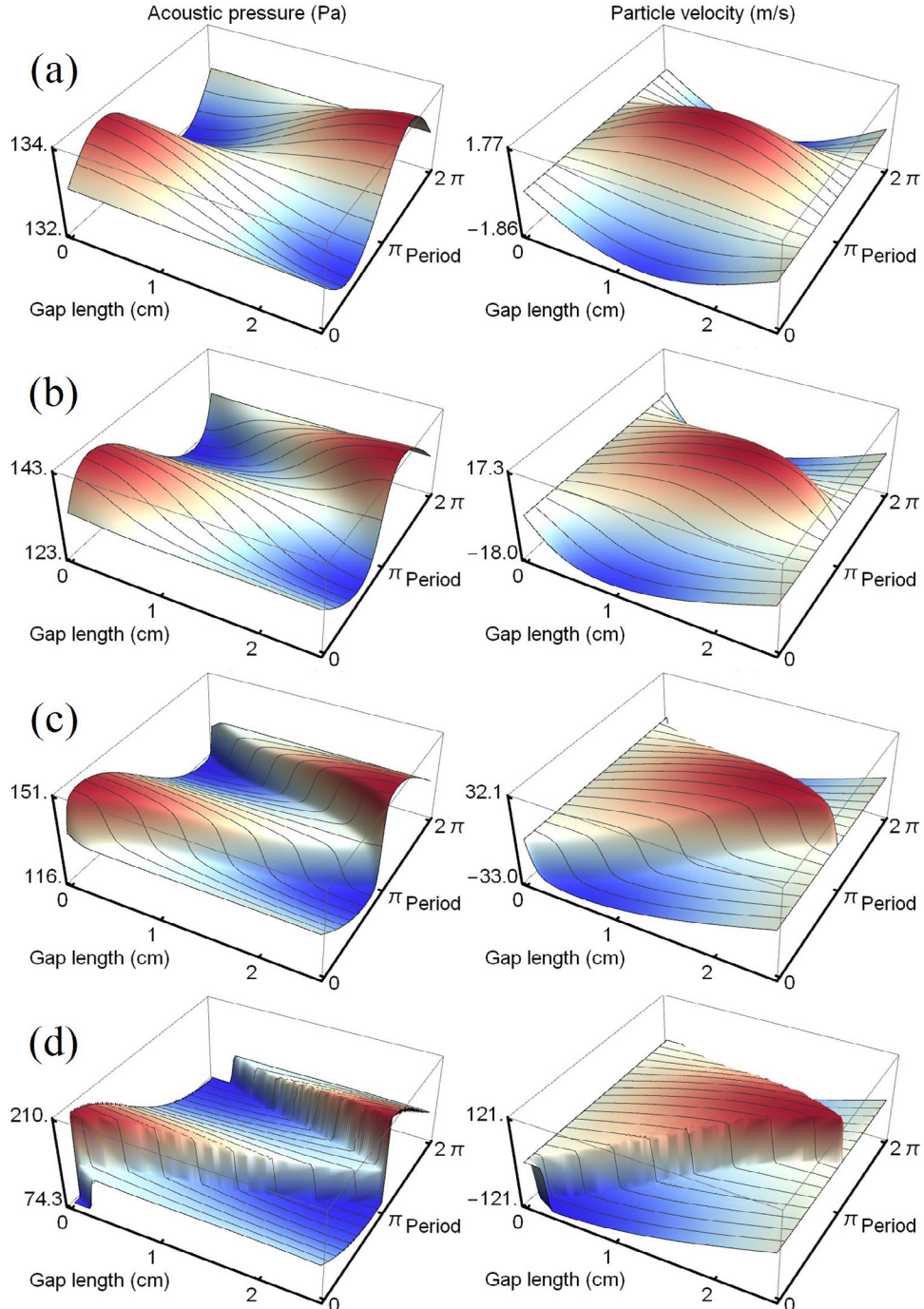


**Figure 2.** The spatiotemporal variation profiles of the acoustic pressures and the particle velocities within one acoustic standing wave period at different vibration amplitudes  $\delta_0$  of (a)  $1 \mu\text{m}$ , (b)  $10 \mu\text{m}$ , (c)  $20 \mu\text{m}$ , and (d)  $200 \mu\text{m}$ .

velocity is more than  $120 \text{ m s}^{-1}$ . These values are expected to be beneficial to the transport of the heavy species and the reactions in the plasma discharges. Therefore, the vibration amplitude  $\delta_0$  is set as  $200 \mu\text{m}$  in the following calculations.

Figures 3 and 4 illustrate the spatiotemporal variation profiles of the electron density  $n_e$  and the  $\text{Ar}^m$  number density  $n_{\text{Ar}^m}$  without and with an acoustic standing wave modulation in one acoustic period. Without the acoustic standing waves, the number density profiles show little fluctuation in an acoustic period, the maximums of  $6.5 \times 10^{16} \text{ m}^{-3}$  for  $n_e$  and  $1.4 \times 10^{19} \text{ m}^{-3}$  for  $n_{\text{Ar}^m}$  are achieved at the center of the

chamber (figures 3(a) and 4(a)). However, with an acoustic field of figure 2(d), the plasma discharge behavior is significantly influenced (figures 3(b) and 4(b)) and a periodically steady state similar to the nonlinear acoustic pressure variation of figure 2(d) is achieved. To indicate the origin of the plasma modulation effect, the influences of the acoustic pressure variation or the particle velocity are numerically ‘switched off’, i.e. setting  $p = 1 \text{ Torr}$  or  $u_n = 0 \text{ m s}^{-1}$  in the calculation with an acoustic standing wave, respectively (results not shown here). It is found that the plasma modulation effect could be primarily attributed to the particle velocity field, which produces

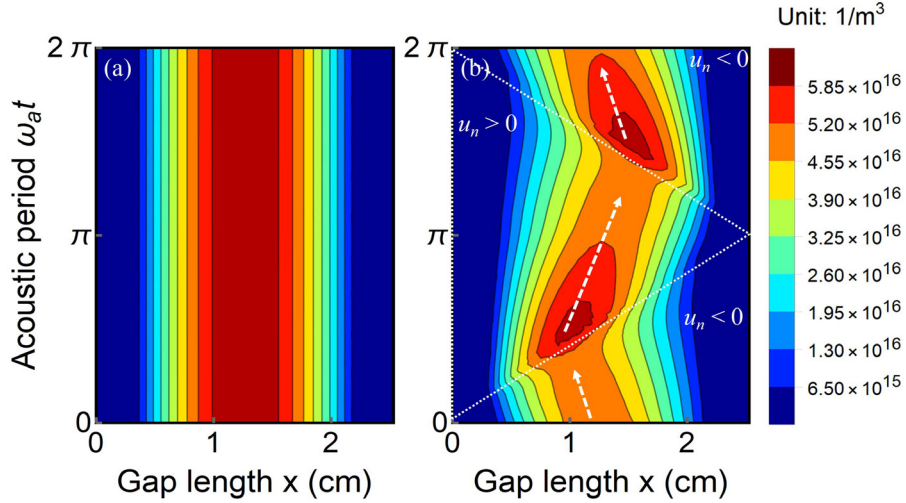


**Figure 3.** The spatiotemporal variation profiles of the electron density  $n_e$  (a) without and (b) with an acoustic standing wave modulation in one acoustic period, at the acoustic field of figure 2(d).

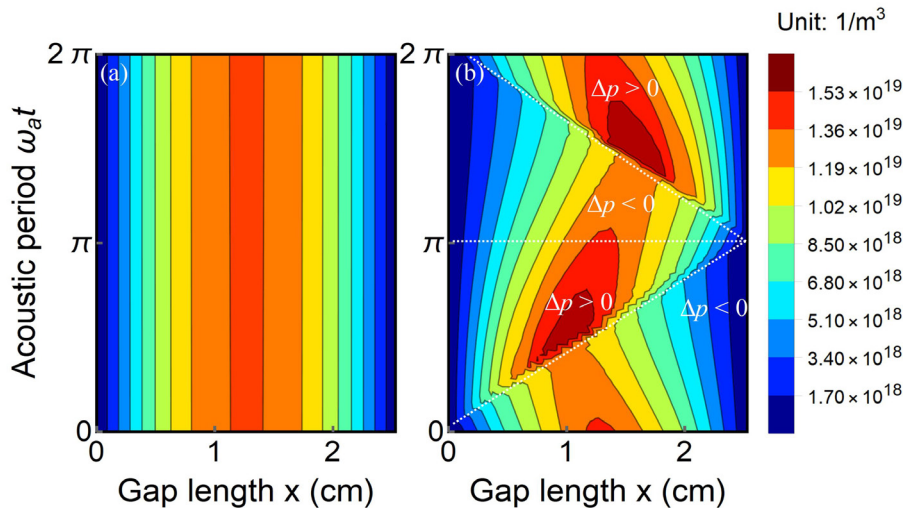


**Figure 4.** The spatiotemporal variation profiles of the  $\text{Ar}^m$  number density (a) without and (b) with an acoustic standing wave modulation in one acoustic period, at the acoustic field of figure 2(d).

a neutral flux friction to the plasma species, and secondarily to the variation of the neutral gas density, which contributes to a nonuniform ionization and excitation rate proportional to the gas density  $n_{\text{Ar}}$ . The transient maximums of  $n_e$  and  $n_{\text{Ar}^m}$  shift with time, as indicated by the white dotted arrows in figure 3(b). By identifying the  $u_n > 0$  region with a white dotted triangle according to figure 2(d), while other regions are  $u_n < 0$  (figure 3(b)), it can be clearly seen that the movement direction of the maximal  $n_e$  and  $n_{\text{Ar}^m}$  is controlled by the particle velocity direction. The charged and activated species in the  $u_n > 0$  region move to the right electrode since they are exerted by a neutral gas friction to the right, and vice versa. Figure 4(b) indicates the regions where the pressure variation  $\Delta p > 0$  and  $\Delta p < 0$ , according to figure 2(d). The number densities of  $n_e$  and  $n_{\text{Ar}^m}$  increase as the profiles evolve from the  $\Delta p < 0$  region into the  $\Delta p > 0$  region, in which the neutral

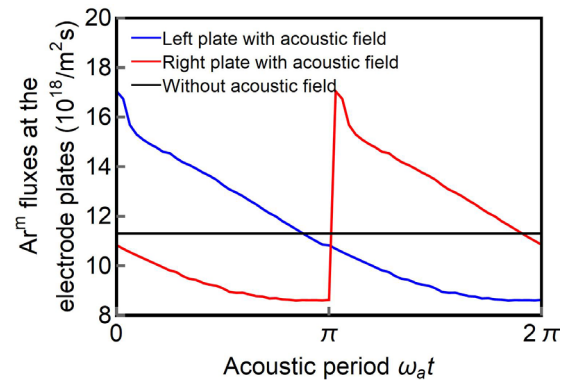


**Figure 5.** The  $\text{Ar}^m$  flux at the electrodes with and without the acoustic standing wave field in one acoustic period, blue: at the left electrode plate, red: at the right electrode plate, black: without an acoustic field.

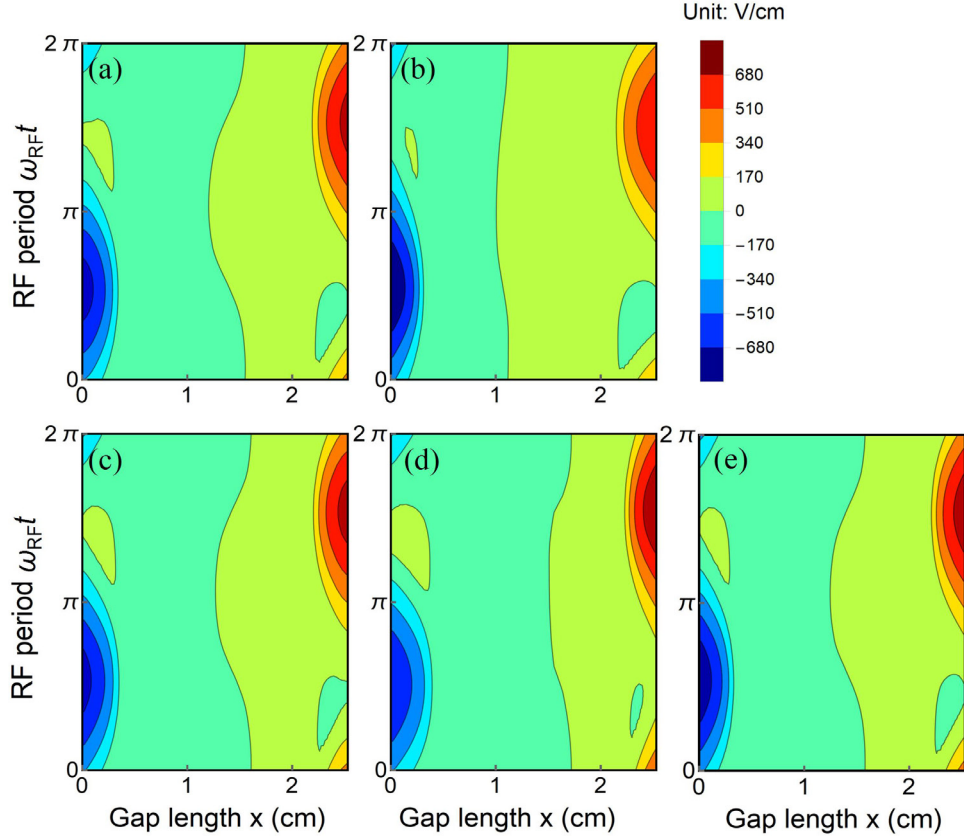


**Figure 6.** The spatiotemporal variation profiles of the electric field in one RF period with an acoustic standing wave modulation at different acoustic-period time moments of (a)  $\omega_a t = 0$ , (b)  $\omega_a t = \pi/2$ , (c)  $\omega_a t = \pi$ , (d)  $\omega_a t = 3\pi/2$ , and (e) without the acoustic modulation.

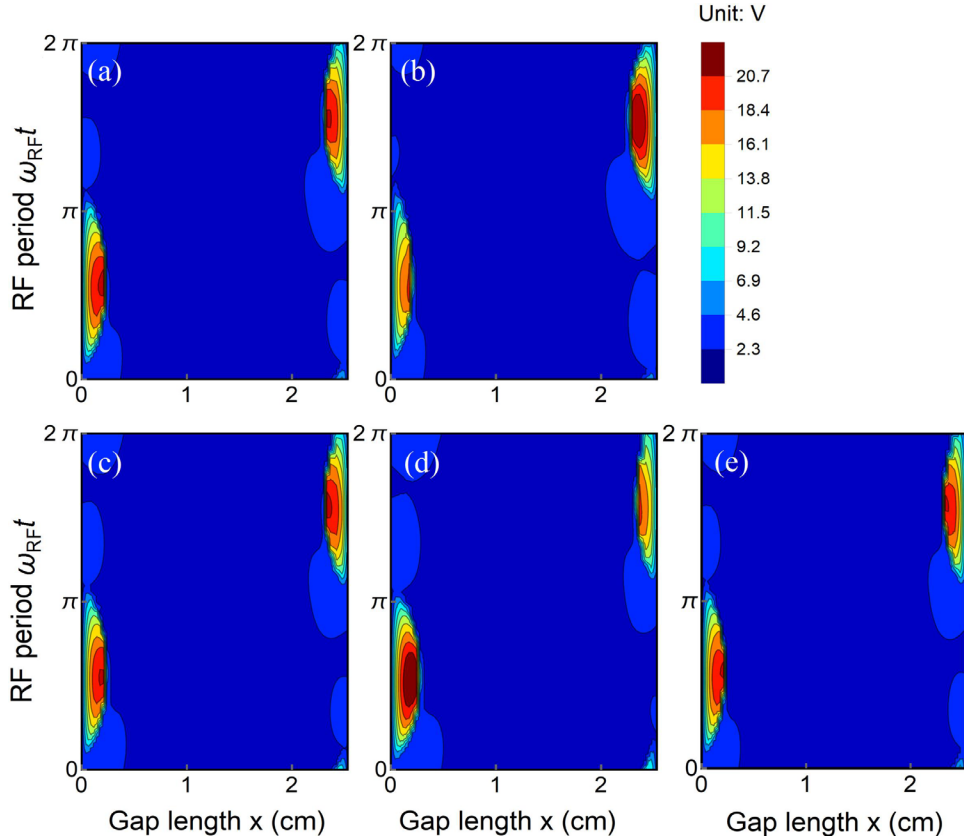


**Figure 7.** The spatiotemporal variation profiles of the electron temperature in one RF period with an acoustic standing wave modulation at different acoustic-period time moments of (a)  $\omega_a t = 0$ , (b)  $\omega_a t = \pi/2$ , (c)  $\omega_a t = \pi$ , (d)  $\omega_a t = 3\pi/2$ , and (e) without the acoustic modulation.

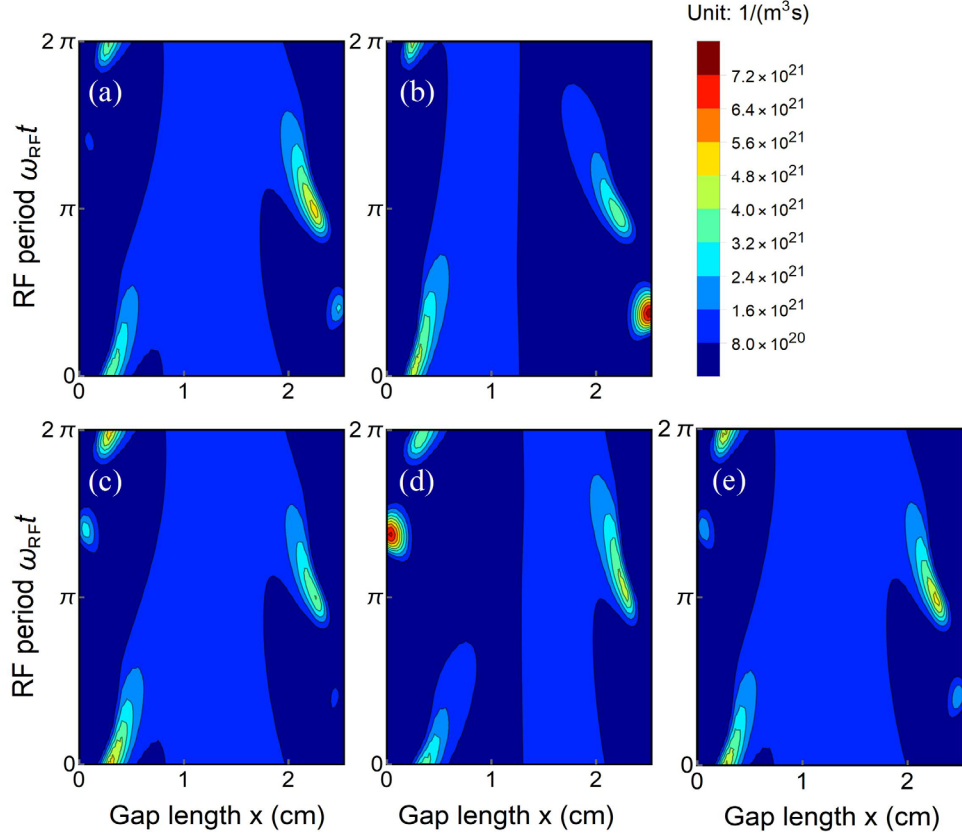


**Figure 8.** The spatiotemporal variation profiles of the ionization rate in one RF period with an acoustic standing wave modulation at different acoustic-period time moments of (a)  $\omega_a t = 0$ , (b)  $\omega_a t = \pi/2$ , (c)  $\omega_a t = \pi$ , (d)  $\omega_a t = 3\pi/2$ , and (e) without the acoustic modulation.

gas density  $n_{Ar}$  is dramatically increased. The maximum of  $n_e$  is barely changed with an acoustic modulation, however, the maximal  $n_{Ar^m}$  in one acoustic period is nearly  $1.7 \times 10^{19} \text{ m}^{-3}$ , about 21% higher than the maximum without an acoustic field. These maximums appear at  $x = 1 \text{ cm}$ ,  $\omega_a t = \pi/2$  and  $x = 1.5 \text{ cm}$ ,  $\omega_a t = 3\pi/2$ , i.e. the turning points of the movement direction, where the maximal acoustic pressure meets the maximal number densities.

The modulation effect is also reflected in the excited species fluxes impinging onto the electrodes/substrates. Figure 5 shows the  $Ar^m$  flux at the electrodes with and without the acoustic standing wave field in one acoustic period. Without the acoustic field, a steady flux of about  $11.3 \times 10^{18} \text{ m}^{-2} \text{ s}^{-1}$  is obtained at both the electrode plates. However, with the acoustic field, the fluxes vary periodically, whose peak reaches up to twice of the minimum value, and there is a phase difference of  $\pi$  between the fluxes at the left and the right electrode plates. Compared with figures 4(b) and 2(d), one can see that the fluxes are proportional to the number density of  $Ar^m$  and the acoustic pressure at the electrode plates, which is natural. The time-averaged fluxes over one acoustic period are basically the same as the fluxes without an acoustic field. However, the pulse nature of the acoustic-wave-modulated fluxes could be beneficial to the plasma processes that need transient high fluxes. In addition, a higher uniformity could be achieved in the propagation direction of the acoustic standing wave. The ion flux at the electrodes are not strongly influenced by the acoustic field (not shown here). However, an effective

modulation could be achieved by coupling with other modulation methods. For example, in the etching processes with a pulsed plasma source, an enhanced negative ion flux to the substrate by diffusion during the pulse-off time [2] could be expected with a synchronized acoustic standing wave, since both the pulsing and the acoustic wave periods could be in the same time scale of tens to hundreds of  $\mu\text{s}$ .

Since the RF source frequency  $f_{RF}$  is much higher than the acoustic frequency  $f_a$ , the acoustic pressure and the particle velocity remain nearly unchanged over one RF period. That means the discharge characteristics vary from one RF period to another, depending on the time moment at which the RF periods are in an acoustic period. To further investigate the influence of an acoustic standing wave on plasma discharges, the modeling results in RF time scales are given and described below. Figures 6 and 7 illustrate the spatiotemporal variation profiles of the electric field and the electron temperature in one RF period with an acoustic standing wave modulation at different acoustic-period time moments of  $\omega_a t = 0, \pi/2, \pi$  and  $3\pi/2$ , as well as without the acoustic modulation. As shown in figure 6, the electric fields remain around zero in the bulk plasma, and change rapidly in the presheath and sheath regions. At  $\omega_a t = \pi/2$ , the plasma density is higher near the left electrode and lower near the right electrode, resulting in the sheath and presheath to be narrower on the left and wider on the right (figure 6(b)). At  $\omega_a t = 3\pi/2$ , the plasma density variation is opposite, as well as the sheath dynamics (figure 6(d)). As shown in figure 7, the electrons are accelerated by

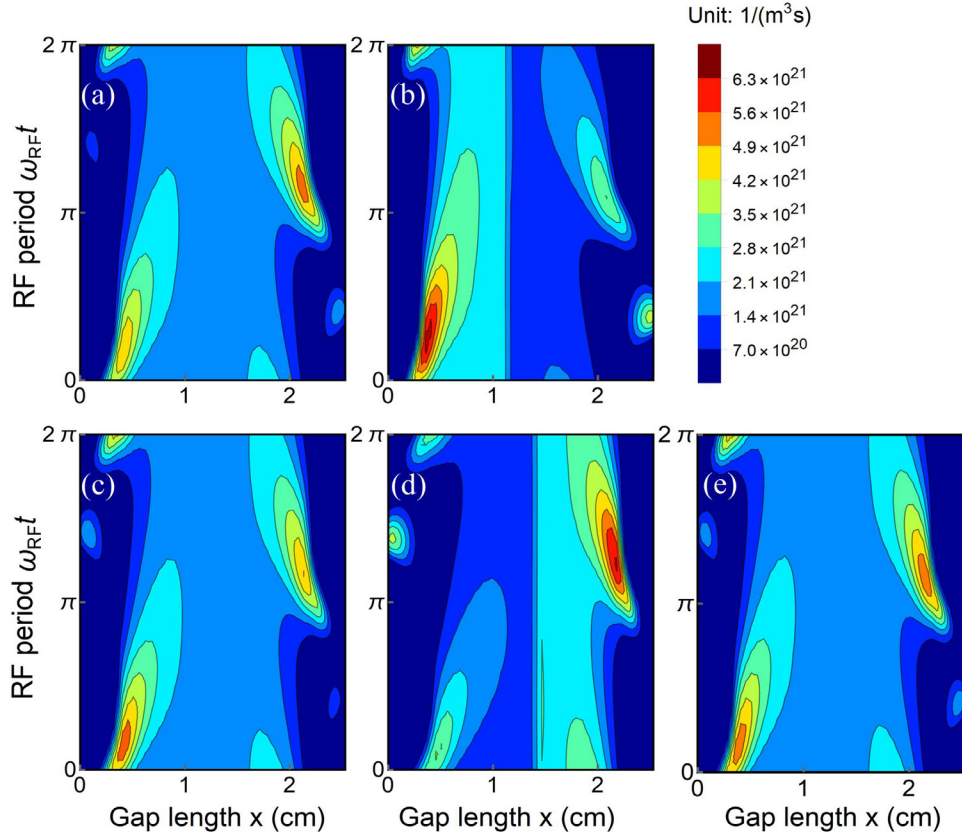


**Figure 9.** The spatiotemporal variation profiles of the excitation rate in one RF period with an acoustic standing wave modulation at different acoustic-period time moments of (a)  $\omega_a t = 0$ , (b)  $\omega_a t = \pi/2$ , (c)  $\omega_a t = \pi$ , (d)  $\omega_a t = 3\pi/2$ , and (e) without the acoustic modulation.

the strong electric fields in the sheath and achieve a high electron temperature, especially in the wider sheaths, where the electrons are more fully accelerated. Besides the maximums of  $T_e$  in the sheaths, there are several local  $T_e$  extremums at  $\omega_{\text{RF}}t = 0$  and  $\omega_{\text{RF}}t = 3\pi/2$  on the left electrode, and at  $\omega_{\text{RF}}t = \pi/2$  and  $\omega_{\text{RF}}t = \pi$  on the right electrode. These extremums are enhanced with the sheath width as well. The local  $T_e$  extremums at  $\omega_{\text{RF}}t = \pi/2$  and  $\omega_{\text{RF}}t = 3\pi/2$  are induced by the local minimum electric field region near the right electrode at  $\omega_{\text{RF}}t = \pi/2$  and the local maximum electric field region near the left electrode at  $\omega_{\text{RF}}t = 3\pi/2$  (figure 6). The local  $T_e$  extremums at  $\omega_{\text{RF}}t = 0$  on the left side and at  $\omega_{\text{RF}}t = \pi$  on the right side are due to the electron heating at the sheath boundaries caused by the sheath expansion. The profiles of the electric field and the electric temperature without an acoustic modulation (figures 6(e) and 7(e)) are between the above extremes.

Figures 8 and 9 illustrate the spatiotemporal variation profiles of the ionization and excitation rates in one RF period at different time moments in an acoustic period. From figure 8, one can see that several ionization sources appear in the regions corresponding to the local  $T_e$  extremums. Recalling that the ionization rate  $R_e = \sum_j k_{iz,j} n_j n_e$  and the ionization rate coefficient  $k_{iz}$  are strongly influenced by  $T_e$ , the striped ionization rate maximums on the left side at  $\omega_{\text{RF}}t = 0$  and on the right side at  $\omega_{\text{RF}}t = \pi$  can be attributed to the positions where the electron temperatures are sufficiently high and the electrons have not been ruled out completely. While the ionization sources

opposite to the sheaths, i.e. on the right side at  $\omega_{\text{RF}}t = \pi/2$  and on the left side at  $\omega_{\text{RF}}t = 3\pi/2$ , are attributed to the local electron temperature maximums as shown in figure 7. For the acoustic period times at  $\omega_a t = 0$  and  $\omega_a t = \pi$  (figures 8(a) and (c)), the acoustic pressure is close to uniform and higher ionization rate appear in the center of the bulk plasma, where the electron density is higher, resulting in a distribution similar to the ionization rate without an acoustic modulation (figure 8(e)). However, the acoustic pressure on the left side of the simulation region is much higher at  $\omega_a t = \pi/2$  and lower at  $\omega_a t = 3\pi/2$ , resulting in a weak ionization rate between  $8 \times 10^{20} \text{ m}^{-3} \text{ s}^{-1}$  and  $16 \times 10^{20} \text{ m}^{-3} \text{ s}^{-1}$  on the center-left position at  $\omega_a t = \pi/2$  (figure 8(b)) and on the center-right position at  $\omega_a t = 3\pi/2$  (figure 8(d)). Similar characteristics can be observed for the excitation rate as shown in figure 9. However, since the excitation rate coefficient  $k_{\text{ex}}$  is less sensitive to the electron temperature compared with  $k_{iz}$ , the excitation rate distribution is less nonuniform than the ionization rate.

The spatiotemporal variation profiles of the power density in one RF period at different time moments of an acoustic period are presented in figure 10. The power density distributions and magnitudes at different time moments are similar to the ionization (figure 8) and excitation (figure 9) rates, demonstrating that the power deposition is modulated by the variation of the background pressure, e.g. the power density is enhanced at  $\omega_a t = \pi/2$  on the left side and at  $\omega_a t = 3\pi/2$  on the right side, which is one of the origins of the acoustic modulation effect to the plasmas.

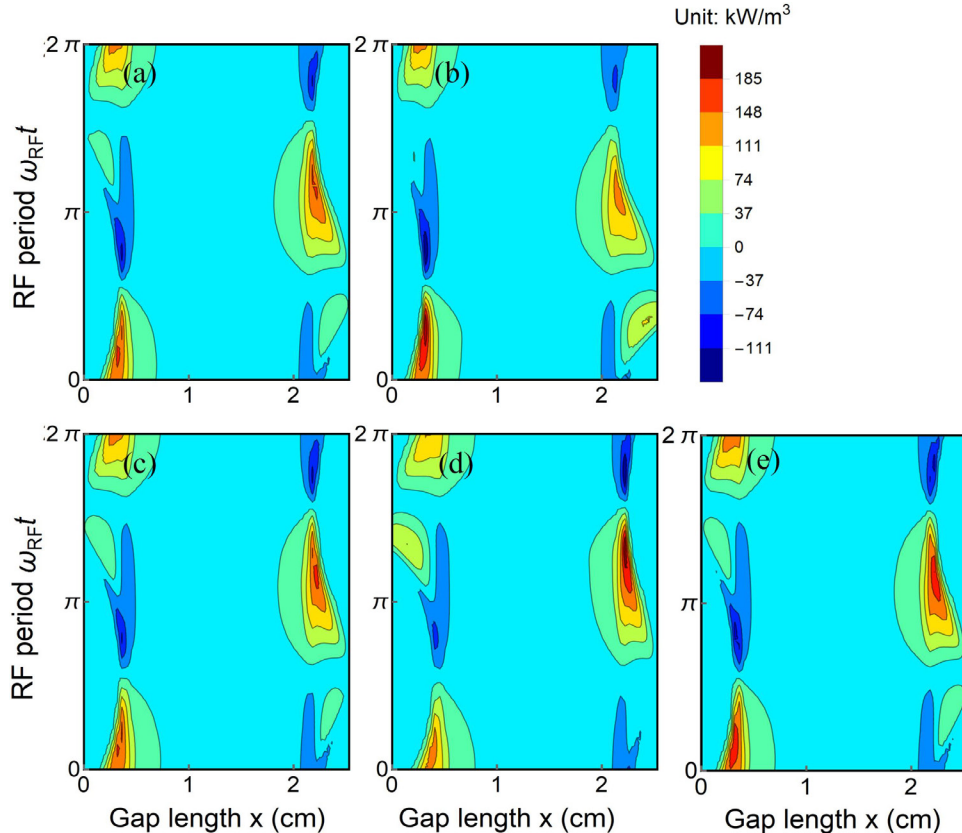


**Figure 10.** The spatiotemporal variation profiles of the power density in one RF period with an acoustic standing wave modulation at different acoustic period time moments of (a)  $\omega_a t = 0$ , (b)  $\omega_a t = \pi/2$ , (c)  $\omega_a t = \pi$ , (d)  $\omega_a t = 3\pi/2$ , and (e) without the acoustic modulation.

#### 4. Conclusions

A 1D self-consistent fluid model has been combined with an acoustic standing wave model to investigate the transient discharge behaviors in a capacitively coupled argon plasma. The acoustic modulation effects have been illustrated by comparing the spatiotemporal distributions of number densities of plasma species with and without the acoustic standing waves in one acoustic period, as well as the spatiotemporal distributions of the electric field, the electron temperature, the ionization and excitation rates, and the power density in one RF period at different time moments in an acoustic period.

The acoustic standing waves have significant influences on the discharge behaviors. When there are no acoustic standing waves in the discharge region, a steady state argon plasma is established with maximal number densities of the electron and the metastable Ar atom at the center of the discharge region. However, by applying an acoustic standing wave, the plasma achieves a periodical steady state similar to the nonlinear acoustic pressure variation, primarily due to the neutral flux friction to the plasma species and secondarily due to the variation of neutral gas density. With the modulation of the acoustic standing waves, a pulsed excited species flux can be obtained at the electrodes, whose maximum value is up to twice of the minimum value. The ion flux at the electrodes are not strongly influenced by the acoustic field. The plasma modulation effect by acoustic standing waves has also been investigated in the RF timescale at different time moments in

an acoustic period. The ionization and excitation rate distributions in one RF period are significantly influenced by the acoustic standing waves, due to the variation of the neutral gas density and the electron temperature.

The different discharge behaviors obtained with and without the acoustic standing waves indicate an obvious modulation effect. In addition, a pulsed excited species flux can be obtained at the substrates. These results contribute to the understand of the mechanism and characteristics of plasma discharges coupled with a high-intensity acoustic standing wave field, as well as the development of plasma modulation methods by acoustic principles. These effects have some implications for the ion extraction, the plasma uniformity and the plasma chemical reactions, which are important for modulating and optimizing the plasmas for plasma etching and plasma enhanced chemical vapor deposition applications. These potential applications will be investigated in the future work.

#### Acknowledgment

This work was partly supported by the National Science Foundation awards #1700785, #1700787 and #1724941.

#### ORCID iDs

Bocong Zheng <https://orcid.org/0000-0002-6052-3693>

## References

- [1] Lieberman M A and Lichtenberg A J 2005 *Principles of Plasma Discharges and Materials Processing* (New York: Wiley)
- [2] Economou D J 2014 *J. Phys. D: Appl. Phys.* **47** 303001
- [3] Jia W-Z, Wang X-F, Song Y-H and Wang Y-N 2017 *J. Phys. D: Appl. Phys.* **50** 165206
- [4] Liu R, Liu Y, Jia W and Zhou Y 2017 *Phys. Plasmas* **24** 013517
- [5] Lafleur T, Delattre P A, Johnson E V and Booth J P 2012 *Appl. Phys. Lett.* **101** 124104
- [6] Vernhes R, Zabeida O, Klemborg-Sapieha J E and Martinu L 2006 *J. Appl. Phys.* **100** 063308
- [7] Ahnood A, Suzuki Y, Madan A and Nathan A 2012 *Thin Solid Films* **520** 4831
- [8] Kim D, Lee S, Kim B, Kang B J and Kim D 2011 *Curr. Appl. Phys.* **11** S43
- [9] Chen F 2016 *Introduction to Plasma Physics and Controlled Fusion* (Berlin: Springer)
- [10] Colas D F, Ferret A, Pai D Z, Lacoste D A and Laux C O 2010 *J. Appl. Phys.* **108** 103306
- [11] Yanallah K, Pontiga F, Bouazza M R and Chen J H 2017 *J. Phys. D: Appl. Phys.* **50** 335203
- [12] Boeuf J P and Pitchford L C 2005 *J. Appl. Phys.* **97** 103307
- [13] Rickard M, Dunn-Rankin D, Weinberg F and Carleton F 2005 *J. Electrost.* **63** 711
- [14] Xu X, Feng J, Liu X-M, Wang Y-N and Yan J 2013 *Vacuum* **92** 1
- [15] Bálek R, Cervenka M and Pekárek S 2014 *Plasma Sources Sci. Technol.* **23** 035005
- [16] Lawrenson C C, Lipkens B, Lucas T S, Perkins D K and Doren T W V 1998 *J. Acoust. Soc. Am.* **104** 623
- [17] Ilinskii Y A, Lipkens B, Lucas T S, Doren T W V and Zabolotskaya E A 1998 *J. Acoust. Soc. Am.* **104** 2664
- [18] Bednarik M and Cervenka M 2014 *J. Acoust. Soc. Am.* **135** EL134
- [19] COMSOL Multiphysics 5.3 2017 *Plasma Module User's Guide* (Stockholm: COMSOL)
- [20] Passchier J D P and Goedheer W J 1993 *J. Appl. Phys.* **74** 3744
- [21] Stewart R A, Vitello P, Graves D B, Jaeger E F and Berry L A 1995 *Plasma Sources Sci. Technol.* **4** 36
- [22] Lymberopoulos D P and Economou D J 1993 *J. Appl. Phys.* **73** 3668
- [23] Gudmundsson J T and Thorsteinsson E G 2007 *Plasma Sources Sci. Technol.* **16** 399
- [24] Lee M-H and Chung C-W 2005 *Phys. Plasmas* **12** 073501
- [25] Ashida S, Lee C and Lieberman M A 1995 *J. Vac. Sci. Technol. A* **13** 2498
- [26] Kannari F, Obara M and Fujioka T 1985 *J. Appl. Phys.* **57** 4309
- [27] Georgieva V et al 2016 *Plasma Process. Polym.* **14** 1600185
- [28] Graves R E and Argow B M 1999 *J. Thermophys. Heat Transfer* **13** 337
- [29] Chapman S and Cowling T G 1970 *The Mathematical Theory of Non-Uniform Gases: An Account of the Kinetic Theory of Viscosity, Thermal Conduction and Diffusion in Gases* (Cambridge: Cambridge University Press)
- [30] Kestin J, Knierim K, Mason E A, Najafi B, Ro S T and Waldman M 1984 *J. Phys. Chem. Ref. Data* **13** 229
- [31] Younglove B A and Hanley H J M 1986 *J. Phys. Chem. Ref. Data* **15** 1323
- [32] Rossing T D 2014 *Springer Handbook of Acoustics* (Berlin: Springer)